

Grant Elliott

Biomechatronics Group,
Department of Electrical Engineering
and Computer Science,
Massachusetts Institute of Technology,
Cambridge, MA 02139
e-mail: gelliott@alum.mit.edu

Andrew Marecki

Biomechatronics Group,
Department of Mechanical Engineering,
Massachusetts Institute of Technology,
Cambridge, MA 02139
e-mail: amarecki@alum.mit.edu

Hugh Herr

Biomechatronics Group,
MIT Media Laboratory,
Massachusetts Institute of Technology,
Cambridge, MA 02139
e-mail: hherr@media.mit.edu

Design of a Clutch–Spring Knee Exoskeleton for Running

Because the leg is known to exhibit springlike behavior during the stance phase of running, several exoskeletons have attempted to place external springs in parallel with some or all of the leg during stance, but these designs have failed to permit natural kinematics during swing. To this end, a parallel-elastic exoskeleton is presented that introduces a clutch to disengage the parallel leg-spring and thereby not constrain swing-phase movements of the biological leg. A custom interference clutch with integrated planetary gear transmission, made necessary by the requirement for high holding torque but low mass, is presented and shown to withstand up to 190 N·m at 1.8 deg resolution with a mass of only 710 g. A suitable control strategy for locking the clutch at peak knee extension is also presented, where only an onboard rate gyroscope and exoskeletal joint encoder are employed as sensory inputs. Exoskeletal electromechanics, sensing, and control are shown to achieve design criteria necessary to emulate biological knee stiffness behaviors in running. [DOI: 10.1115/1.4027841]

1 Introduction

An exoskeleton that successfully modifies human gait to reduce joint loading, muscle fatigue, or metabolic demand of locomotion would have tremendous practical benefit to armed forces burdened by load, to an aging population constrained by joint injury, or as a biomechanics research tool. Yet, despite this utility, metabolic augmentation of human locomotion has proved an elusive goal. For example, while a number of exoskeletons have been built, none has demonstrated a significant reduction in the metabolic demand of locomotion [1]. Here, we present a novel exoskeletal architecture for augmenting running.

It is a long standing result in biomechanics that running most resembles a mass bouncing on a linear spring [2–4]. Gravitational and kinetic energy remain primarily in phase, while elastic energy stored in tendons and other elastic structures contributes an out of phase component. In fact, the ground reaction force during stance phase, when the leg is in contact with the ground, varies approximately linearly with compression of effective leg length [5]. Not surprisingly then, significant predictive power may be obtained from a simple spring–mass model that treats the body as a point mass bouncing on a constant stiffness spring during stance [2]. This effective spring may be considered as either purely vertical and characterized by k_{vert} or subtending an angle as the hip extends and characterized by the smaller k_{leg} . For typical running speeds (3–5 m/s), k_{leg} is on the order of 10 kN/m and varies relatively little with speed [3].

It is critical to note that this effective stiffness is present only while the leg is in contact with the running surface. The leg can be thought of as a two-stiffness system—nearly zero in swing and very stiff in stance. This is observable directly in the torque–angle trajectories of the biological knee (Fig. 1), which resembles that of a clutched spring.

This springlike dynamic of leg joints likely derives in part from passive energy storage, accounting for the efficiency of human running. Tendons and ligaments have been implicated in the energy transfer and storage observed during running stance phase [6–8], though it is important to note that even ideal energy storage

of this kind is not without cost as the series muscle must exert an opposing force to enable tendon stretch. Even a nearly isometric contraction, yielding little or no net mechanical work, incurs a significant metabolic cost [7,9]. Note also that, if the muscle does not act isometrically, the series muscle–tendon system may exhibit a stiffness different from that of the passive tendon alone. Critically, the effective joint stiffness, as determined from the torque–angle relationship during the gait cycle, characterizes the dynamic task but does not necessarily represent an impedance and is therefore more accurately described as a quasi-stiffness [10].

Recently, exoskeletons have sought to emulate this passive elastic architecture for augmentative purposes. One may hypothesize that if the role of tendon and other elastic tissue could be fulfilled externally, series muscle activation could be reduced or eliminated while total kinetics, with the exoskeletal contribution

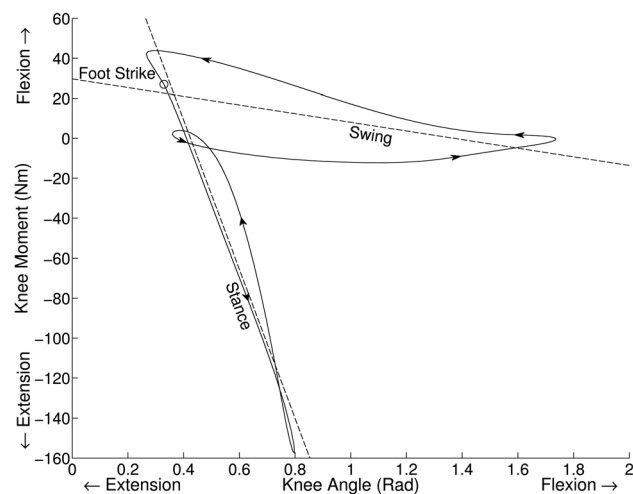


Fig. 1 Torque and angle of the biological knee during unassisted human running. Dashed lines indicate least squares linear fits during stance and swing, showing the two-stiffness knee behavior in running. Data were replotted from Ref. [17].

Manuscript received July 17, 2013; final manuscript received June 2, 2014; published online July 21, 2014. Assoc. Editor: William K. Durfee.

included, are preserved. In fact, there is evidence that total leg stiffness, including external contributions, is maintained in bounding gaits. If a series elasticity, namely, a compliant ground surface, is introduced, total k_{vert} including the series compliant surface is maintained [11,12], even when doing so requires increasing biological leg stiffness by up to 68%. This adaptation is extremely fast, occurring within the very first step after transition to the compliant surface [13].

A parallel-elastic leg exoskeleton was first proposed by Yagn in 1890 [14] (Fig. 2(a)). Though never demonstrated, the device sought to augment running and jumping by transferring loads through external passive springs in parallel with each leg, thereby unburdening the biological joints. Without a mechanism to permit knee flexion and swing phase, however, such a device is impractical in natural running. Even so, a very similar device (Fig. 2(b)), also without any mechanism for disengaging the spring, has proven effective in reducing the metabolic demand of hopping [15]. Compellingly, biological leg stiffness was found to decrease in the presence of the parallel spring in order to achieve the necessary k_{vert} , even when the external spring is nonlinear [15]. The observed decrease in metabolic cost is hypothesized to be due to a decrease in activation of the ankle plantar flexors and knee extensors. Similarly, if a passive spring is placed only across the ankle joint during hopping, total leg stiffness, k_{leg} , and total ankle quasi-stiffness, including the exoskeletal contribution, are both regulated [16].

Unfortunately, these entirely passive spring exoskeletons preclude natural gait. Normal gait kinematics are incompatible with the passive knee extension or ankle plantar flexion that is externally enforced. For example, in the hopping exoskeleton, a passive spring spanning the knee resists knee flexion during swing, requiring increased energy expenditure either at the knee to compress the spring or at the hip first to abduct then to adduct while swinging the leg with increased moment of inertia.

This problem is resolved if the bow spring may collapse at an exoskeletal joint during swing phase, providing no elastic force, but subsequently lock prior to stance. Such a device permits a normal swing phase while augmenting stance phase as the hopping exoskeleton does. Moreover, this architecture is robust in that it may be repurposed to span one or several joints of the leg, as demonstrated in Fig. 3. This paper presents such a spring-clutch exoskeleton. Because the holding torque and mass specifications for such a device cannot be simultaneously achieved using a

commercially available clutch, in this paper, we also present the design of a custom interference clutch with an integrated planetary gearbox.

An architecture for such an exoskeleton was derived from the existing hopping exoskeleton with improved human attachment and elastic elements. Specifications for the exoskeletal joint were derived from existing biomechanical data and a custom high torque; low mass clutch was designed and fabricated. This design was then validated both by simulation and by physical loading. In addition to the clutch design, we also present the design of a control system to enable clutch locking and unlocking throughout a running gait cycle. Human running experiments are conducted to evaluate control system functionality.

2 Methods

The problem of constructing a spring-clutch exoskeleton may be divided into five components: human attachment, the energy storing elastic element, the clutched exoskeletal joint, electronics, and control.

2.1 Human Attachment. Load-bearing attachment to the human body poses several problems. First, there is a question of which joints the exoskeleton's spring should span. Subsequently, the problem of attachment itself is made particularly daunting by the compressibility of soft tissue and the ability of skin to translate relative to the underlying skeleton during motion.

In principle, a harness needs simply to connect the body's center of mass to the ground through the passive compliance offered by the exoskeleton without slipping during the high bandwidth impact, but any number of geometries may accomplish this goal. Since all devices of this type span the knee, energy is stored during early stance knee flexion and returned during late stance extension. Energy storage due to motion in other joints depends on the choice of architecture and, in particular, on whether the proximal attachment of the spring spans the hip and whether the distal attachment spans the ankle. Each attachment requires a different style of harness.

Figure 4 schematically depicts several exoskeleton geometries. Figure 4(b) represents a harness like that used in the elastic hopping exoskeleton [15], in which the pin joints connect the spring proximally to a rigid pelvic harness concentric to the biological hip joint and distally to a shoe close to the toe. In Fig. 3(a), the

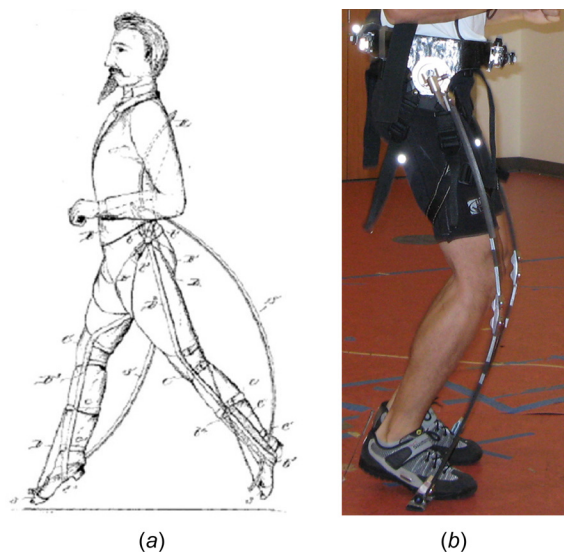


Fig. 2 Parallel elastic lower limb exoskeletons. (a) Yagn's concept [14] and (b) MIT's hopping exoskeleton [15].

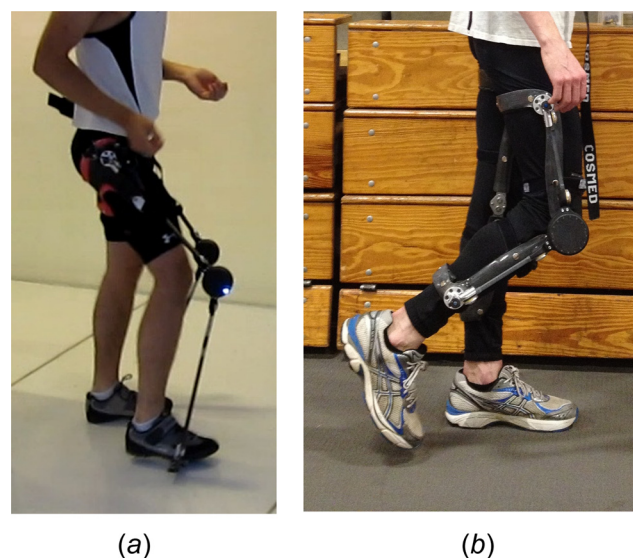


Fig. 3 Two configurations of the quasi-passive elastic exoskeleton. (a) Spanning the knee and ankle (as in Fig. 4(b)). (b) Spanning only the knee (as in Fig. 4(a)).

pelvic harness has been replaced by molded carbon fiber thigh cuffs which are attached to neoprene shorts using straps which closely follow the skin's lines of nonextension. This design offers greater hip mobility, less discomfort, and a significant reduction in mass. Most importantly, the proximal attachment point is far less able to move axially up the leg under load, increasing energy storage in the elastic element.

This attachment requires a toe-striking gait, which is more natural in hopping than in running. To accommodate heel or midfoot striking, one may bypass the ankle and contact the ground directly, as in Fig. 4(c), though this requires an additional two-degrees of freedom with spring return so that the distal termination floats in the sagittal plane. A simpler solution is to attach to the body proximal to the ankle, as in Fig. 4(a), with the attachment point likely integrated into a knee or ankle brace to limit migration of the harness up the leg. This is demonstrated in Fig. 3(b), using an elongated polycentric carbon fiber knee brace. On either side of the knee, the exoskeleton applies load to the leg through rubber-lined carbon fiber cuffs. Care has been taken to remove material from the cuffs in areas in which muscle bellies may protrude, most notably around the hamstrings and gastrocnemius. Rigid carbon fiber strips back the brace at its most proximal and distal extents and independently adjustable velcro straps secure the brace to the leg both anterior and posterior at four heights (two proximal and two distal).

In both cases, the exoskeletal springs are attached laterally to the thigh cuffs. Lateral mounting allows the springs not only to follow the form of the leg relatively closely but also widens the wearer and produces a larger than normal torque in the coronal plane during stance. For these reasons, efforts have been made to

reduce the lateral displacement of the exoskeleton as much as possible.

2.2 Elastic Element Design. The elastic element of the exoskeleton consists of thin strips of semirigid unidirectional "E" fiberglass laminate located proximal and distal to the lockable exoskeletal joint. The net system constitutes a compression spring, characterized by the geometry of these elastic elements. In particular, it may be shown that torque in the spring is proportional to the elastic modulus of the material and the second moment of area of the cross section about the neutral axis, which for a rectangular cross section is proportional to the leaf spring's width and the cube of the leaf's thickness. Because these leaves are planar, they may be easily manufactured in a variety of materials, thicknesses, widths, and lengths using a water jet cutter.

While varying elastic modulus and cross section allows for variation of spring stiffness, the form of the force-distance relationship depends on spring and attachment geometry. It is possible to design springs ranging from nearly linear to highly nonlinear using a model of spring deformation. As the deformations experienced exceed those typically considered in small angle approximations, finite element analysis is used to characterize the net spring. The geometry of the knee brace configuration shown in Fig. 3(b) is found to produce slightly sublinear torsional springs (that is, torque increases disproportionately slowly compared to displacement), as shown in Fig. 5. Specifically, torque is approximately proportional to angular displacement to the power of 0.87. Based on such simulations, leaf springs were manufactured with average stiffnesses ranging from 25 N-m/rad to 150 N-m/rad (although limitations of the current harness design preclude the use of stiffnesses in excess of 50 N-m/rad).

2.3 Clutched Exoskeletal Joint. As shown in Fig. 1, the human knee experiences torques which may exceed 150 N-m during the stance phase of running [17]. Assuming that the exoskeleton geometry is similar to that of the natural leg, the proposed exoskeletal joint should be rated to loads of at least this in order to permit any of the various attachment configurations described in Sec. 2.1 though, in practice, the natural leg will still bear a significant fraction of this load, rendering the rating conservative. With some safety margin then, 200 N-m was decided upon as a holding torque specification. Moreover, due to the high metabolic demand of forward swing and the corresponding necessity for a low moment of inertia about the hip, the joint must permit the full range of biological knee flexion (up to 135 deg in fast running)

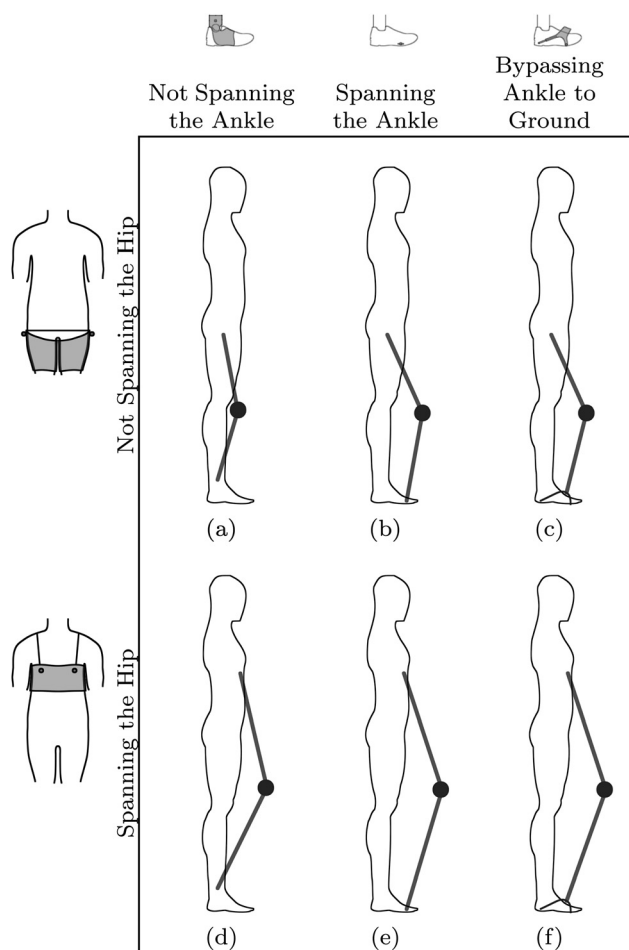


Fig. 4 Possible configurations of the clutched parallel elastic exoskeleton by combination of proximal and distal attachments

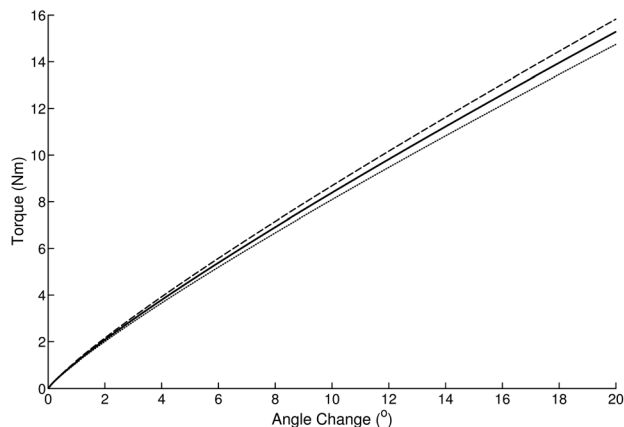


Fig. 5 Simulated torque applied to the knee by the spring geometry shown in Fig. 3(b) as a function of change in knee angle, starting from knee angles of 15 deg (- - -), 20 deg (—), and 25 deg (- · - · -). Note that torque increases slightly sublinearly with angle and is weakly dependent on the initial knee angle when the clutch is locked.

Table 1 Design specifications for the exoskeletal joint

| Description | Goal | Achieved |
|---|------|----------|
| Holding torque (T) (N·m) | 200 | 190 |
| Radial load (F_r) (N) | 3000 | 4780 |
| Axial load (F_a) (N) | 1000 | 4050 |
| Engagement time (Δt_{eng}) (ms) | 50 | 28.6 |
| Resolution (deg) | 2 | 1.8 |
| Range of motion (deg) | 135 | 130 |
| Mass (g) | 1000 | 710 |
| Diameter (mm) | 100 | 85 |
| Thickness (mm) | 50 | 49 |

and contribute as little distal mass to the leg as possible. Using the known influence of increased leg mass on walking as a guide [18], 1 kg was determined to be the maximum allowable mass of the exoskeletal joint. Unfortunately, as shown in Fig. 13, these specifications for holding torque and mass exceed the capabilities of any commercially available clutches even before considering the mass of housing, instrumentation, and electronics, necessitating the design of a custom clutch.

Several additional specifications constrain the design, as enumerated in Table 1. If the elastic element is to load directly to the ground, the joint must be able to withstand radially the full load seen by the human leg in running—typically three body weights [3]—as well as a smaller off axis component determined by the angle formed by the leg with the ground. The exoskeletal joint must also lock precisely at peak knee extension, immediately before the swing-phase retraction which precedes foot strike, to ensure that the spring begins deforming immediately at foot strike and maximum energy is stored. As total knee flexion during stance is approximately 25 deg [17] and energy storage in a linear spring goes as the square of angle, an engagement error of just 5 deg corresponds to a greater than one-third decrease in energy storage. Consequently, the device must offer a high resolution of potential locking angles, compared to total knee flexion during

stance, and must be capable of engaging quickly, compared to the speed of terminal swing knee flexion. Finally, the entire package must be in a form factor compatible with the human knee.

The exoskeletal joint consists of an interference clutch (chosen for its high ratio of holding torque to mass) in series with a planetary gearbox which decreases load on the clutch plates and increases effective resolution, compensating for the discretized engagement of the interference clutch. The complete device, depicted schematically in Fig. 6, is constructed so that the distal bow spring attachment serves as input to the ring of a planetary system whose planet carrier is fixed to the proximal assembly. The output of the planetary system (the sun) is coupled through a toothed clutch to the proximal assembly, effectively locking the joint when the clutch is engaged by activation of a solenoid.

The clutch is integrated with the gearbox and control electronics as tightly as possible to minimize mass and bounding box without compromising ease of maintenance. Only the medial clutch plate translates, while only the lateral clutch plate rotates, in order to simplify bearing design. As can be seen Fig. 7, the linear plain bearings, which support the translating plate, are located between the planetary gears, while a pair of ball bearings support the sun and rotating clutch plate. The sun gear itself is hollow, allowing the solenoid which actuates the clutch to be placed within it. Radial and axial forces are borne by a pair of opposing angular contact ring bearings supporting the distal spring attachment and ring gear.

Electronics, discussed in Sec. 2.4, are housed in a lateral sub-assembly with only a single pair of wires necessary to connect to the solenoid. A quadrature phase encoder for measuring exoskeletal joint angle and a break beam for measuring solenoid position are both interfaced optically. The sensor suite is completed by a three-degrees-of-freedom sagittal plane inertial measurement unit.

Because the clutch is designed to be engaged at zero relative velocity, a mechanical synchronizer is omitted in favor of a predictive software synchronizer, discussed in Sec. 2.5, capable of precisely timing engagement. A sawtooth topology further compensates for the lack of a mechanical synchronizer by ensuring

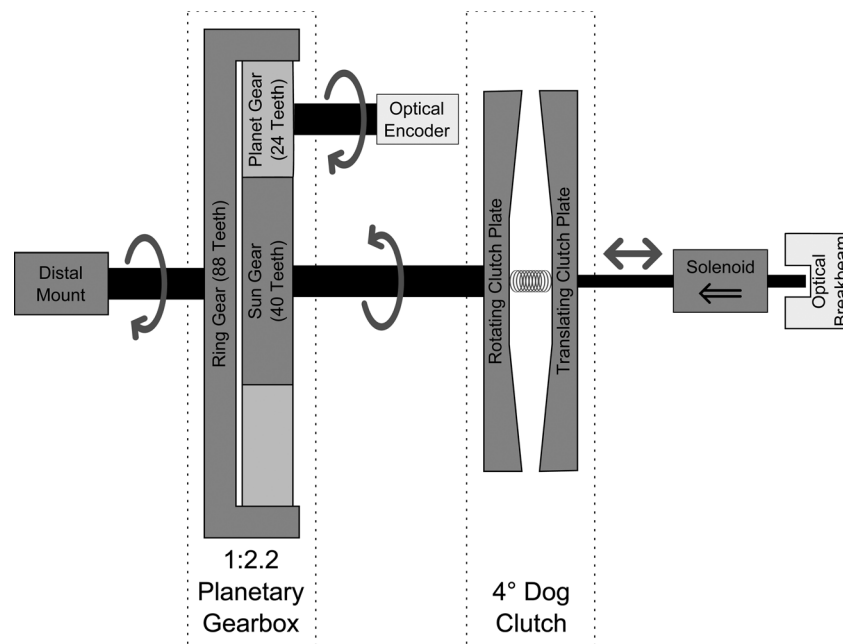


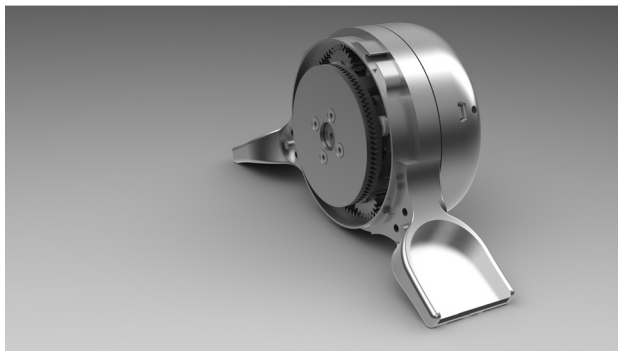
Fig. 6 Schematic depiction of the designed exoskeletal joint, showing the clutch, integrated planetary gearbox, and instrumentation. The system, including the orbit of the planetary gearbox, is depicted as mechanically grounded to the proximal mount, so that flexion of the knee corresponds to rotation of distal mount. With the clutch engaged, the distal mount cannot rotate relative to the proximal mount, forcing the leaf spring to flex instead. Note that though the actual device is functionally equivalent to this depiction, its construction varies significantly.



(a)



(b)



(c)

Fig. 7 Renders of the left exoskeletal joint showing integration between the subsystems. (a) Lateral assembly removed to show encoder disk, solenoid, and translating mechanism. (b) Lateral planet carrier removed to show planetary gearbox and linear bearings containing bosses of the translating clutch plate. (c) Reverse angle with medial components removed to show rotating (foreground) and translating clutch plates in the disengaged state.

that during partial engagement an energy gradient exists which tends to align and fully engage the clutch. To minimize wear, the sharp roots and tips of the teeth are filleted. Unfortunately, this also introduces an unengaged unstable equilibrium, but in practice any movement of the device remedies this potential problem. Sawteeth also permit a ratcheting effect; when engaged, the joint cannot be flexed, but extension remains possible. Consequently, control strategies may err in favor of early engagement before the knee has reached peak extension. (Deliberately doing so is not a reasonable strategy, however. Extension of the joint during clutch engagement is somewhat impeded and presumably contributes a non-negligible metabolic cost.)

Parameters of the clutch plates are given in Table 2. The clutch plates are produced in titanium to minimize weight and two different alloys (grades 2 and 5) are used to reduce galling. The geometry of the clutch plates is constrained both by tight integration

Table 2 Clutch parameters

| Description | Value |
|---|---------|
| Clutch plate tooth count (N_c) | 90 |
| Clutch plate tooth height (h_c) | 2.0 mm |
| Clutch plate tooth width (w_c) | 1.5 mm |
| Clutch plate tooth depth (d_c) | 6.5 mm |
| Clutch plate tooth inner radius ($r_{i,c}$) | 22.5 mm |
| Clutch plate tooth outer radius ($r_{o,c}$) | 29.0 mm |

with the planetary gearbox and by manufacturing requirements. Notably, these parts are manufactured by contour milling, enforcing a minimum base fillet at the inner radius of 1/64 in. and thereby limiting the resolution to 4 deg (90 teeth).

The geometry of the integrated planetary gearbox is heavily constrained by the need to accommodate the solenoid within the sun gear and the linear bearings between the planets. The transmission is characterized by parameters given in Table 3. Once again, to avoid galling, the ring and sun are specified as grade 5 titanium, while the planets are specified as grade 4. (In fabricating the prototype presented here, grade 2 titanium was used in lieu of grade 4, derating the device somewhat.) These spur gears were manufactured by wire electrodischarge machining.

The housing of the exoskeletal knee joint is entirely aluminum and capable of withstanding unexpected impacts with the environment in the course of normal use.

2.4 Electrical Systems. The lateral cap of the exoskeletal knee comprises an electronics subassembly, including a custom printed circuit board (PCB) and 2000 mA-h single cell lithium polymer battery. A single pair of wires connects the electronics subassembly to the solenoid; all sensors are either confined to the circuit board or interfaced optically. An AtMega168PA AVR microcontroller operating at 12 MHz monitors the onboard sensors (listed in Table 4) and controls the exoskeletal knee. A set of 16 light-emitting diodes (LEDs), directed to the face of the lateral subassembly by light pipes, provides visual indication of state while more complete diagnostic logs are available through USB tethering or may be recorded on an onboard MicroSD card for later analysis.

A three-degrees of freedom inertial unit comprising a dual-axis microelectromechanical systems (MEMS) accelerometer and a MEMS gyroscope provides acceleration and rotation rate sensing within the sagittal plane. The accelerometers are primarily used to assess foot strike. Because the circuit board is fixed to the proximal assembly, the gyroscope is indicative of hip rotational velocity and is used to assess midswing and midstance. Rotation rate in midswing is particularly informative as an indication of running velocity.

Rotation of the clutch is measured using a reflective optical encoder. The quadrature phase disk is mounted to one of the planets rather than directly to the distal subassembly, both to accommodate the solenoid at the center of the device and to obtain an effective increase in resolution from the higher speed of the

Table 3 Transmission parameters

| Description | Value |
|---|--------|
| Planetary transmission ratio (R_t) | 2.2 |
| Number of planets (P_t) | 4 |
| Planetary spur gear module (m_t) | 0.8 mm |
| Planetary spur gear pressure angle (ϕ_t) | 20 deg |
| Planetary spur gear face width (f_t) | 6.0 mm |
| Number of teeth on sun (N_s) | 40 |
| Number of teeth on planet (N_p) | 24 |
| Number of teeth on ring (N_r) | 88 |

Table 4 Sensors used in the exoskeletal knee.

| Measurement | Part | Technology | Interface | Resolution | Range | Bandwidth |
|---|--|--------------------|-----------|------------------------|----------------------|-----------|
| Anterior–posterior acceleration Superior–inferior acceleration | ADIS16006 | MEMS accelerometer | SPI | 0.038 m/s ² | ±49 m/s ^s | 100 Hz |
| Sagittal plane angular rate | ADIS16100 | MEMS gyroscope | SPI | 1.12 deg | ±1380 deg/s | 185 Hz |
| Exoskeletal knee angle | E4P (disk) AEDR (reader) LS7336R (counter) | Reflective encoder | SPI | 0.068 deg | 0–135 deg | |
| Clutch engagement distance | EE-SX1109 | Break beam | Analog | 0.1 mm | 0–2 mm | |

planets. It aligns with the PCB-mounted reader when the lateral subassembly is installed.

The solenoid which engages the clutch is driven by a 46.9 kHz pulse width modulated signal with 8-bit resolution. Solenoid position feedback is obtained from an infrared break beam sensor soldered to the PCB interacting with an aluminum flag machined into the solenoid mount. This flag is dimensioned such that the sensor saturates when the cage is completely disengaged, but provides analog sensing over the final 2 mm of engagement, including any partial tooth engagements. This sensor is nonlinear and exhibits slight hysteresis. For practical purposes, it offers 0.1 mm resolution.

The complete system draws approximately 17 mW to power the microcontroller, 129 mW to power sensors, and an average of 540 mW to power the solenoid (all values calculated). Accounting for switching converter efficiencies, total battery draw is approximately 860 mW, allowing the onboard battery to power the device for approximately 8 h.

2.5 Control Strategy. In order to maximize energy storage in the spring without constraining the leg at toe-off, the controller should produce full engagement at the time of maximum knee extension shortly before foot strike and full disengagement prior to toe-off. Ideally, each exoskeletal knee achieves this independently and requires no extrinsic inputs. The controller is implemented within a framework developed with prosthetic and orthotic systems in mind. The control problem itself is divided into two primary components: analyzing the gait cycle using kinematic sensing and compensating for the electromechanical latency of the clutch. Additionally, a pulse and hold strategy is implemented to reduce power consumption in the solenoid once the clutch is fully engaged.

These systems are implemented using a proprietary development framework, updated at 750 Hz. During each update, sensors are read into memory, an internal state machine is advanced, solenoid feedback is calculated, the solenoid and LED hardware is updated, and debug data are logged. Each phase of this process is individually monitored by watchdog timers and a hardware failure or software timeout triggers a “kill” mode which disables the exoskeleton, maintaining it in the disengaged, zero-stiffness state. Notably, this framework has the property that the user space accessible to the controls designer allows interaction exclusively with memory, never directly with hardware.

Using the exoskeletal knee encoder and the sagittal plane gyroscope as surrogates for biological knee angle and hip velocity during swing phase (see Table 5 for variable notation), the state machine shown in Fig. 8 suffices to interpret the phases of this gait:

- (1) **Preswing:** Toe-off completes, the knee flexes in order to minimize its moment of inertia for forward swing, and the hip begins to flex accelerating the leg forward. Positive rotation of the gyroscope exceeding $\dot{\psi}_{\text{swing}}$ causes transition to swing 1.
- (2) **Swing 1:** The knee continues to flex, eventually achieving maximum flexion. Once the exoskeletal knee angle has

extended beyond its observed maximum flexion by a hysteresis band $\Delta\theta_{\text{flexion}}$, the state machine advances to swing 2.

- (3) **Swing 2:** The knee begins to extend in preparation for foot strike. The solenoid latency compensation algorithm is activated. Once the projected time to maximum knee extension Δt_{eta} is less than the known clutch engagement time Δt_{eng} and the exoskeletal knee angle has decreased by at least $\Delta\theta_{\text{swing}}$, the solenoid is activated and the state machine progresses to terminal swing.
- (4) **Terminal Swing:** The clutch engages shortly before the foot touches the ground. Vertical acceleration in excess of \ddot{y}_{strike} at impact causes transition to early stance.
- (5) **Early Stance:** The biological knee flexes while the ankle dorsiflexes, resulting in a shortening effective leg length. With the clutch engaged, the exoskeletal knee does not flex and the bow spring bears load, storing energy. The hip flexes, propelling the body forward. The resulting negative rotation of the gyroscope in excess of $\dot{\psi}_{\text{stance}}$ causes deactivation of the solenoid and transition to terminal stance.
- (6) **Terminal Stance:** The center of mass reaches its lowest point, after which the biological knee and ankle reverse direction, resulting in a lengthening effective leg length. Although the solenoid is off, the clutch is bound by the large applied torque. As toe-off nears, the effective leg length approaches and eventually exceeds that when the clutch was engaged, allowing it to relax to its disengaged state. The detection of this disengagement by the break beam sensor causes transition to preswing.

The solenoid is activated, using a pulse and hold strategy informed by the optical break beam to reduce power consumption, while in the terminal swing and early stance states.

If the clutch were able to engage without delay, the swing 2 state could simply monitor for a minimum in the knee encoder and engage the clutch immediately as it transitions to terminal swing. In practice, a significant latency is associated with the electromechanical system comprising the solenoid, return spring, and translating clutch plate. Experimentally, the delay from application of 24 V to the solenoid to full engagement of the clutch is

Table 5 Variables related to exoskeletal knee control, grouped into direct sensor readings and calculated internal state

| Symbol | Description | Units |
|---------------------------|---------------------------------------|------------------|
| \ddot{x} | Anterior–posterior acceleration | m/s ² |
| \ddot{y} | Superior–inferior acceleration | m/s ² |
| $\dot{\psi}$ | Sagittal plane angular velocity | deg/s |
| θ | Exoskeletal knee angle | deg |
| λ | Scaled optical break beam reading | |
| Δt_{state} | Time since last state change | ms |
| Δt_{eta} | Predicted time to peak knee extension | ms |
| η | Fractional clutch engagement | |

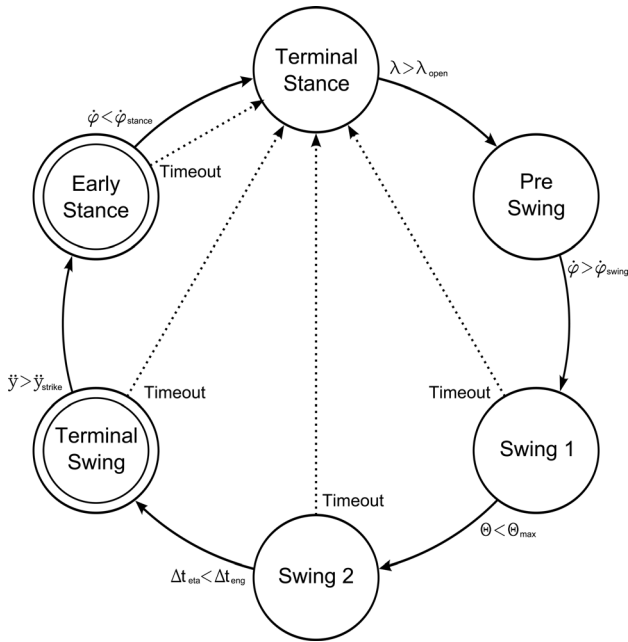


Fig. 8 State machine that controls the exoskeletal knee clutch. See Sec. 2.5 for an explanation of state exit conditions.

approximately 30 ms. As this time is comparable to the duration of late swing, it is necessary to compensate for the electromechanical latency, firing the solenoid early to ensure that the clutch is fully engaged at the time of maximum knee extension. The latency compensation algorithm in use during the swing 2 state is a resolution to this difficulty.

Consider only late swing phase between peak knee flexion and foot strike (isolated by the state machine presented). During this phase, knee angle is approximately parabolic so we may fit the observed encoder counts to a second order polynomial with peak knee extension at the vertex. Using such a continuously generated fit, we elect to fire the solenoid once the predicted vertex position is less than 30 ms in the future.

Unfortunately, the entirety of late swing is not parabolic; an inflection point exists that varies substantially between wearers and is in general difficult to predict or identify. As the region before this inflection point would skew the regression, the fit is performed on a running window rather than to all data in late swing.

While a closed form to a quadratic least squares regression exists (and in fact can be computed only from running sums), we use a simpler, even less computationally expensive solution. Rather than fitting encoder readings to a quadratic and seeking the vertex, we fit differentials of encoder readings to a line and seek the zero crossing. It may be shown that updating such a least squares fit and determining the expected number of samples until the zero crossing (corresponding to the knee extremum) requires the maintenance of only a single running sum and involves no radical calculations, making it extremely inexpensive computationally.

It is worth noting that this latency problem exists in the biological system as well, as muscle force develops on the order of 50 ms after the onset of activity observed by electromyography (which in turn is delayed by nerve conduction velocity). Consistent with this, electromyographic activity is observed in the quadriceps approximately 78 ms prior to foot strike, allowing sufficient time for muscle force development prior to contact [4].

2.6 Testing Methodology. The final device's resolution, range of motion, and physical dimensions are totally specified by the design while radial and axial loading specifications are derived directly from the ratings of the supporting bearings. Determining

the clutched exoskeletal joint's engagement time and maximum holding torque is more difficult, however.

Engagement time was determined experimentally. The microcontroller was used to repeatedly apply 24 V to the solenoid and measure the time delay before the optical break beam reported the moment of engagement.

In order to determine the maximum holding torque, SolidWorks Simulation (formerly known as COSMOS) was used to perform finite element analysis. Bending was simulated in both clutch and spur gear teeth, while torsion was investigated in the clutch plate body and in the hub of the sun gear which connects the clutch to the gear box. Analytical methods were also used to predict compressive failure of the plain bearings which permit translation of the clutch plate and rotation of the planets.

A clutch of this form is unlikely to fail in shear during full engagement; rather, it will fail due to tooth bending during incomplete engagement. This bending was simulated at a partial engagement of 75% with one plate fixed and the other constrained at its inner diameter, free only to rotate. For this simulation, only the annuluses, where the teeth are located, were modeled. The torque on the clutch at failure was multiplied by the gear ratio to determine the total load at failure.

Bending of the spur gears was simulated independently at the ring-planet interface and the planet-sun interface. All gears were constrained at their bearing surfaces. In both cases, a single planet was simulated, equal loading was assumed, and input torque was determined by gear ratio. Torsion in the disk of the clutch plate was simulated by fixing the mounting bosses and applying torque at the inner radius of the teeth. Similarly, torsion in the hub of the sun gear was simulated by fixing the mounting bosses and applying torque at the base radius of the teeth.

In all cases, failure was determined to have taken place when the tensile yield strength of the material was reached. It is important to note that such a failure is most likely not catastrophic.

The holding torque of the exoskeletal joint was also verified experimentally. With the clutch locked at full extension, the simulated holding torque at yield was applied using masses and a rigid lever arm. Following this loading, the device was disassembled and components were examined for microfractures under an optical microscope. As the device had been used extensively by the time of this test, evidence of galling was also sought.

Finally, the control strategy was verified and its parameters were adjusted during a series of human running trials. Three healthy male subjects, recruited from the research group, ran with the device first on a treadmill with parallel bars and eventually on unrestricted flat terrain. Treadmill running was performed at speeds between 3 and 5 m/s, while unrestricted running was performed at self selected speeds. Data were recorded only from onboard exoskeletal sensors. These experiments were conducted in accordance with MIT Committee on the Use of Humans as Experimental Subjects (COUHES) protocol No. 0801002566.

3 Results

3.1 Mechanical Validation. Experimental testing reveals that engagement time has a mean of 28.6 ms and a standard deviation of 8.3 ms, with some right skew. No engagements requiring in excess of 60 ms were observed. High engagement times were rare and likely represent the unstable equilibrium achieved when tooth fillets collide directly. Though possible in static tests such as this, such an interaction is extremely unlikely in a dynamic environment.

Analytical and simulated maximum holding torque, as limited by various components, are summarized in Table 6. Simulation of the worst expected load on the clutch teeth (90 N·m on the clutch after gear reduction) at 75% engagement is shown in Fig. 9. Yield is predicted at 700 N·m, corresponding to more than 1500 N·m at the output shaft. Analytically, Lewis bending, corrected for contact ratio and load sharing over the planets, predicts yield in the

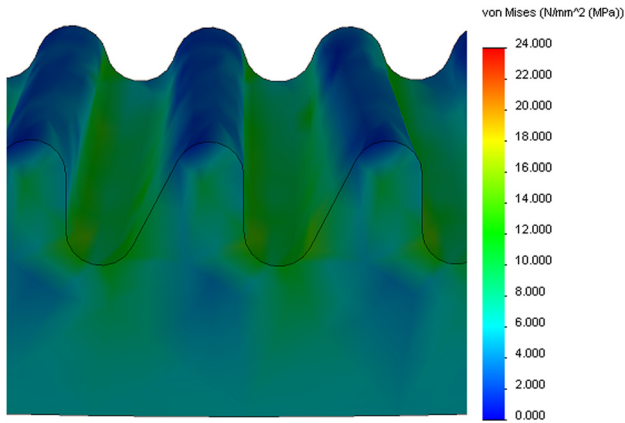


Fig. 9 Finite element analysis of the clutch teeth during 75% partial engagement at maximum expected loading. Failure does not occur as the tensile yield strength of grade 2 titanium is 275 MPa.

Table 6 Maximum exoskeletal joint torque as limited by failures in several components. Results of both conservative analytic calculations and finite element analysis are presented.

| Component | $T_{\max,calc}$ | $T_{\max,fea}$ |
|---|-----------------|----------------|
| Clutch teeth | 480 N·m | 1560 N·m |
| Ring gear teeth | 650 N·m | |
| Planet gear teeth against ring gear teeth | 300 N·m | |
| Planet gear teeth against sun gear teeth | 190 N·m | 190 N·m |
| Sun gear teeth | 290 N·m | |
| Sun gear hub | 2000 N·m | 2070 N·m |
| Clutch plate | 730 N·m | 700 N·m |
| Linear bearing | 1100 N·m | |
| Planet bearing | 310 N·m | |

gearbox first in the planet teeth at the interface to the sun. This result is confirmed by finite element analysis, as shown in Fig. 10. This in fact proves to be the weakest component of the design, limiting the holding torque to 190 N·m. Simulation confirmed that torsion in transmission elements is not a limiting factor in this design, with the bulk of the rotating clutch plate failing with 700 N·m applied to the joint.

Because the fabricated exoskeletal joint uses planet gears made from grade 2 rather than grade 4 titanium, its maximum holding

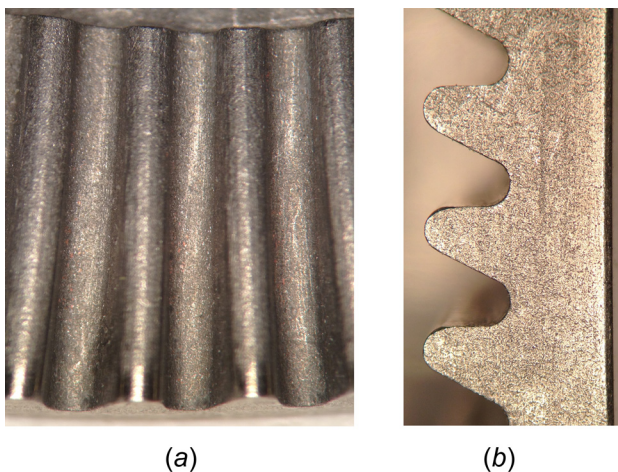


Fig. 11 Clutch plate seen from two perspectives under an optical microscope following load testing: (a) face and (b) edge

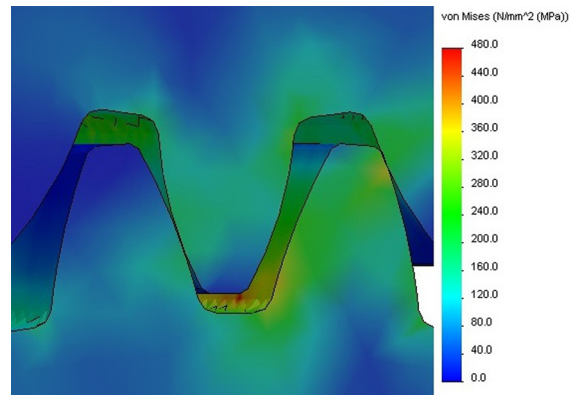


Fig. 10 Finite element analysis of the interface between a planet gear (top) and the sun gear (bottom) at maximum expected loading. Plastic deformation has just begun in the planet, as the tensile yield strength of grade 4 titanium is 480 MPa, while the grade 5 sun gear remains elastic.

torque is derated to 110 N·m by the significantly lower yield modulus of grade 2 titanium. Loading the joint to 110 N·m caused no catastrophic or otherwise visible failure. Examination of a clutch plate (Fig. 11) and a planet (Fig. 12) reveals no evidence of plastic deformation, microfractures, or galling. The device handles load in accordance with simulation results.

The exoskeletal joint, then, exhibits exceptional holding torque for its mass. Even without compensating for the additional mass of housings, electronics, and instrumentation, the exoskeletal joint easily outperforms commercially available devices in this metric, as may be seen in Fig. 13.

3.2 Control Strategy Validation. Figure 14 depicts transitions of the state machine described in Sec. 2.5 and Fig. 8 using exoskeletal angle encoder and sagittal gyroscope data collected during treadmill running. In particular, the state machine successfully activates the latency compensation algorithm during late swing so that the solenoid may be engaged shortly prior to foot strike.

Figure 15 demonstrates the efficacy of the latency compensation algorithm described in Sec. 2.5 during treadmill running with a window 16 samples wide and a look ahead threshold of 30 samples at an update frequency of 800 Hz (note that these parameters are slightly different from the final configuration enumerated in Table 7). The algorithm successfully predicts the time of true

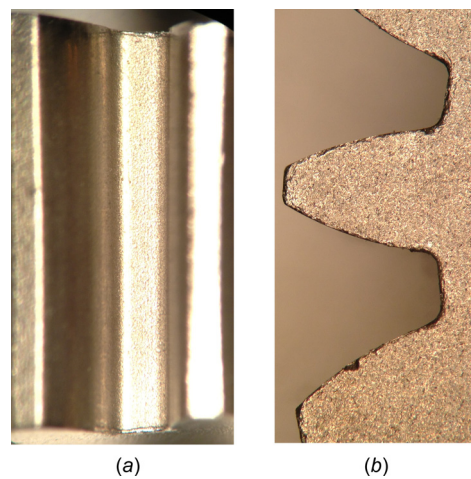


Fig. 12 Planet gear at the interface to the sun gear seen from two perspectives under an optical microscope following load testing: (a) edge and (b) face

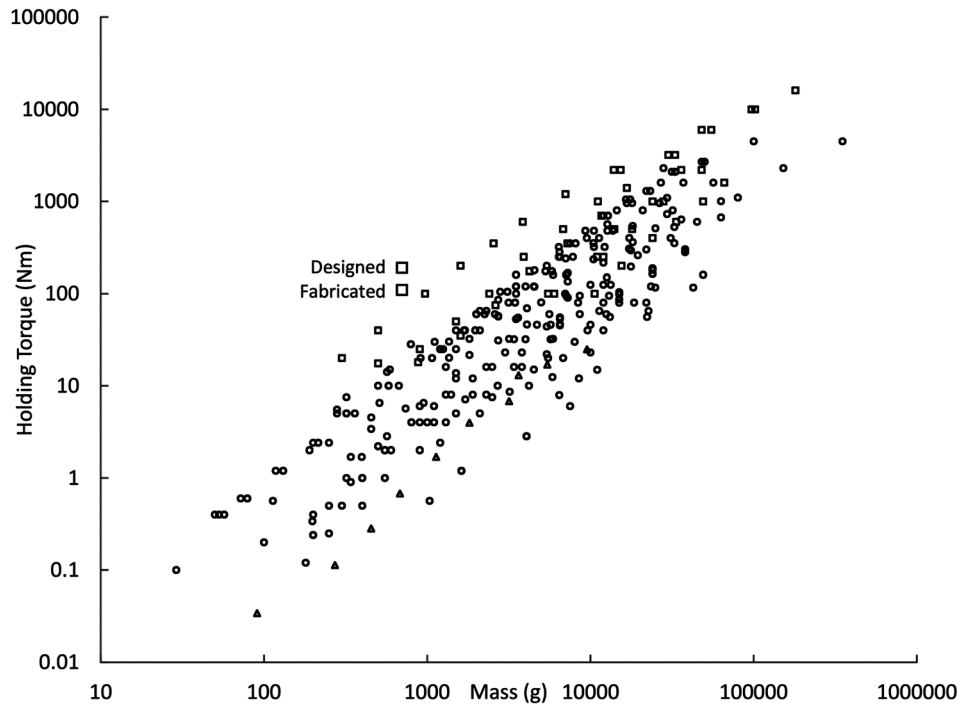


Fig. 13 Maximum holding torque versus mass plotted on log-log axes for several hundred commercially available interference clutches (\square), particle brakes (\triangle), and friction (applied by air, spring, wrap-spring, electromagnet, or permanent magnet) brakes and clutches (\circ). For comparison, both the designed and fabricated exoskeletal joints described here are also shown (large \square), plotted with masses that additionally include electronics, instrumentation, and mounting.

peak knee extension sufficiently far in the future to allow for complete clutch engagement.

4 Discussion

In the design of parallel elastic exoskeletons, a high torque, low mass clutch is critical. Quasi-passive clutches avoid problems of

movement constraint and power consumption, while low mass is necessary to avoid burdening the wearer. These problems are far from unique to exoskeleton design; such a clutch is applicable to a myriad of prosthetic and orthotic applications which similarly require small, lightweight surrogates for nearly isometric muscle activations.

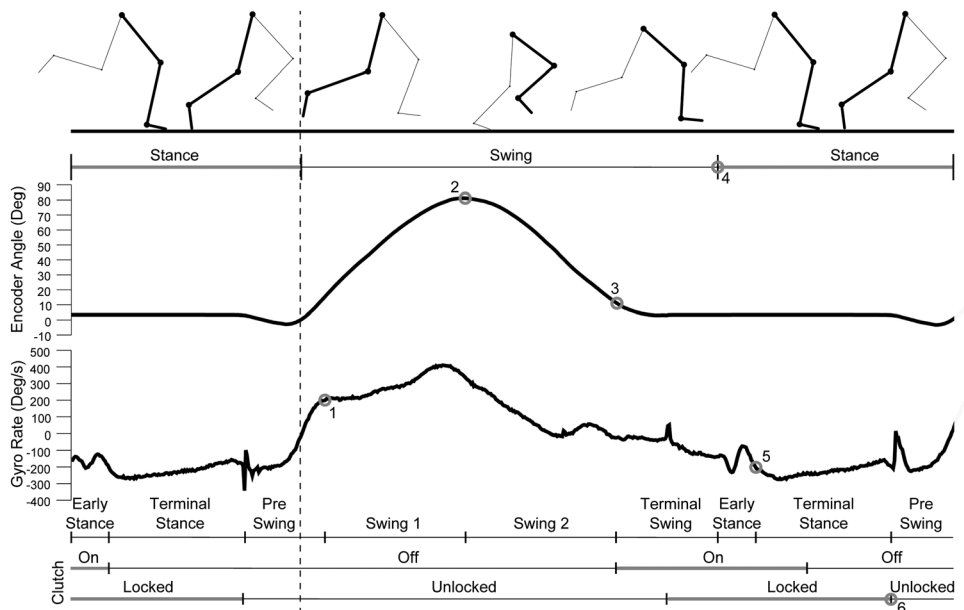


Fig. 14 Depiction of events used to identify and act on phases of the gait cycle using the state machine in Fig. 8. Data shown were recorded during treadmill running from the onboard exoskeletal joint encoder, surrogating biological knee angle during swing, and rate gyroscope, surrogating biological hip rate. Numbered circles indicate state exit transitions. More than one cycle is shown to clarify the periodic nature of the gait.

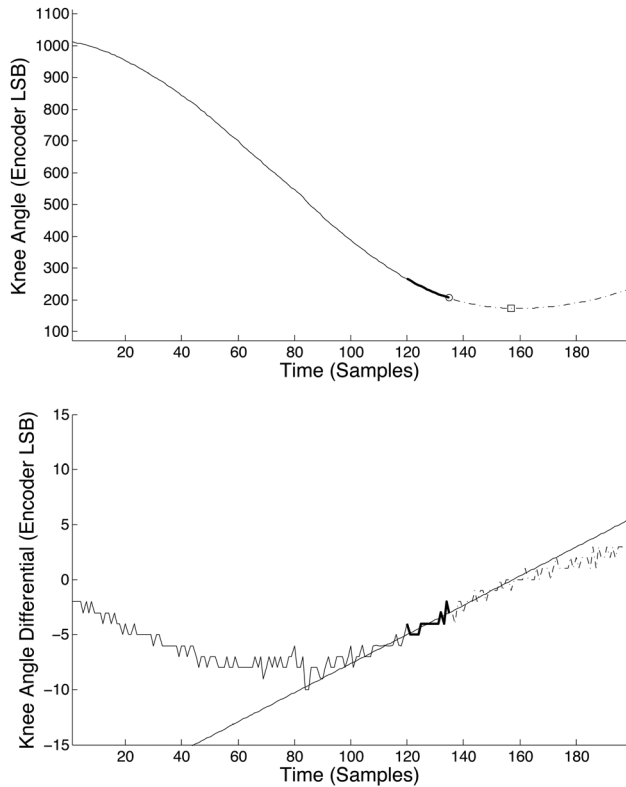


Fig. 15 Demonstration of solenoid latency compensation predicting peak knee extension during the swing phase. Encoder data were recorded at 800 samples per second during treadmill running. The bold region represents the window of data used in the final iteration before firing the solenoid. The firing time is denoted by a circle, while the predicted extremum is denoted by a square. The dotted line denotes data after the time the solenoid is fired. Note the correspondence between the predicted and actual times of peak knee extension.

The trade-off between holding torque and mass is clear from a perusal of commercial products. Given the low demand for lightweight clutches in typical industrial applications, it is perhaps unsurprising that it is possible to exceed the torque–mass performance of commercial offerings through the use of expensive

materials and high precision machining. A more subtle issue exists, however, in the trade-offs necessary to simultaneously achieve high resolution. As may be seen in Fig. 13, for a given mass, the highest torque by far is achieved by interference clutches, which inherently limit resolution to the tooth size. The maximum achievable resolution may be limited by bending of the teeth, but is ultimately limited by machining capabilities. In applications, such as this, a resolution of 4–5 deg, as is typical, is unacceptable.

This device introduces a new trade-off between resolution and complexity. The addition of a planetary transmission grants an increase in resolution, but at a cost of more moving parts, heavily loaded bearings, and complex systems integration. The gearing also increases the rotational inertia and frictional losses of the system. Fortunately, however, this transmission also decreases the load on the clutch, permitting a reduction in its size and mass and granting a further increase in resolution, as the teeth may be made as small as is machinable. Alternatively, resolution could have been increased without the transmission and associated increase in complexity by simply increasing the diameter of the clutch, with consequences in both mass and, more importantly, form factor.

Though it is seldom discussed by commercial vendors designing for high speed operation, it is ultimately this trade-off for resolution which governs the design of the exoskeletal joint. The decision to incorporate a geared transmission has ramifications in manufacturing, operation, and maintenance and was not made lightly, but permits the construction of a high torque, low mass clutch with reduced sacrifice in resolution and form factor.

The clutch–spring exoskeleton presented here permits the addition of parallel stiffness during stance, potentially unburdening joints and muscles, without preventing natural swing, avoiding a critical limitation of past parallel elastic exoskeletons. Doing so requires power only to periodically activate a solenoid (less than 1 W). Moreover, owing to a custom clutch design which integrates an interference clutch with a planetary gearhead, the device contributes an acceptable mass.

The control strategy presented here, based on a state machine and solenoid latency compensation, is extremely reliable in steady state running, with very nearly 100% accuracy, but less so during speed transients or alternate gaits. Notably, undesirable locking of the clutch may occur during rapid deceleration. Though parameters were tuned to inhibit locking during walking, stair descent may bring about undesirable locking as well.

Table 7 Constants related to exoskeletal knee control, grouped into intrinsic hardware properties, tunable parameters, and tunable state machine time constraints

| Symbol | Description | Value |
|--|--|-----------------------|
| f | Update frequency | 750 Hz |
| Δt_{eng} | Clutch engagement time | 30 ms |
| λ_{open} | Optical break beam open threshold | 0.20 |
| λ_{closed} | Optical break beam closed threshold | 0.90 |
| W | Latency compensation window size | 32 |
| $\dot{\psi}_{\text{swing}}$ | Sagittal plane angular velocity swing threshold | 200 deg/s |
| $\dot{\psi}_{\text{stance}}$ | Sagittal plane angular velocity stance threshold | -200 deg/s |
| \ddot{y}_{strike} | Superior acceleration foot strike threshold | 30.0 m/s ² |
| $\Delta\theta_{\text{flexion}}$ | Hysteresis width to detect peak knee flexion | 2 deg |
| $\Delta\theta_{\text{swing}}$ | Minimum knee excursion in swing | 40 deg |
| D_{open} | Solenoid duty cycle while closing | 1.00 |
| D_{closed} | Solenoid duty cycle once closed | 0.24 |
| $\Delta t_{\text{Swing1,max}}$ | Maximum time in swing 1 | 200 ms |
| $\Delta t_{\text{Swing2,max}}$ | Maximum time in swing 2 | 320 ms |
| $\Delta t_{\text{TerminalSwing,max}}$ | Maximum time in terminal swing | 250 ms |
| $\Delta t_{\text{EarlyStance,min}}$ | Minimum time in early stance | 20 ms |
| $\Delta t_{\text{EarlyStance,max}}$ | Maximum time in early stance | 200 ms |
| $\Delta t_{\text{TerminalStance,min}}$ | Minimum time in terminal stance | 20 ms |

In the current system, these problems are largely avoided by manually triggering the exoskeleton's "kill" mode when operation is not desired. They could be addressed more robustly through the addition of states to track other common gaits, such as walking, independently, thereby reducing the reliance on carefully tuned thresholds. Those parameters that are inherently linked to running speed, such as the swing-phase angular velocity threshold, may also be made adaptive, so that the controller may respond better to changing speeds. Indeed, such improvements will be critical to the development of a safe always-on wearable system.

Preliminary investigations into the physiological effects of this exoskeleton on running are noted in Ref. [19].

Acknowledgment

The authors would like to thank Blake Sessions, who contributed significantly to the first generation clutch design, and Luke Mooney, who assisted in the loading test.

References

- [1] Herr, H., 2009, "Exoskeletons and Orthoses: Classification, Design Challenges and Future Directions," *J. NeuroEng. Rehabil.*, **6**(June), p. 21.
- [2] McMahon, T. A., and Cheng, G. C., 1990, "The Mechanics of Running: How Does Stiffness Couple With Speed?" *J. Biomech.*, **23**(S1), pp. 65–78.
- [3] Farley, C. T., and Ferris, D. P., 1998, "Biomechanics of Walking and Running: From Center of Mass Movement to Muscle Action," *Exercise Sport Sci. Rev.*, **26**(1), pp. 253–285.
- [4] Novacheck, T. F., 1998, "The Biomechanics of Running," *Gait Posture*, **7**(1), pp. 77–95.
- [5] Farley, C. T., and Gonzalez, O., 1996, "Leg Stiffness and Stride Frequency in Human Running," *J. Biomech.*, **29**(2), pp. 181–186.
- [6] Biewener, A. A., 1998, "Muscle Function In Vivo: A Comparison of Muscles Used for Elastic Energy Savings Versus Muscles Used to Generate Mechanical Power," *Am. Zool.*, **38**(4), pp. 703–717.
- [7] Alexander, R. M., 1991, "Energy-Saving Mechanisms in Walking and Running," *J. Exp. Biol.*, **160**(1), pp. 55–69.
- [8] Cavagna, G. A., Heglund, N. C., and Taylor, C. R., 1977, "Mechanical Work in Terrestrial Locomotion: Two Basic Mechanisms for Minimizing Energy Expenditure," *Am. J. Physiol. Regul., Integr., Comp. Physiol.*, **233**(5), pp. 243–261.
- [9] McMahon, T. A., 1984, *Muscles, Reflexes, and Locomotion*, Princeton University, Princeton, NJ.
- [10] Rouse, E. J., Gregg, R. D., Hargrove, L. J., and Sensinger, J. W., 2013, "The Difference Between Stiffness and Quasi-Stiffness in the Context of Biomechanical Modeling," *IEEE Trans. Biomed. Eng.*, **60**(2), pp. 562–568.
- [11] Ferris, D. P., 1998, "Running in the Real World: Adjusting Leg Stiffness for Different Surfaces," *Proc. Biol. Sci.*, **265**(1400), pp. 989–994.
- [12] Kerdok, A. E., Biewener, A. A., McMahon, T. A., Weyand, P. G., and Herr, H. M., 2002, "Energetics and Mechanics of Human Running on Surfaces of Different Stiffnesses," *J. Appl. Physiol.*, **92**(Feb.), pp. 469–478.
- [13] Ferris, D. P., Liang, K., and Farley, C. T., 1999, "Runners Adjust Leg Stiffness for Their First Step on a New Running Surface," *J. Biomech.*, **32**(8), pp. 787–794.
- [14] Yagn, N., 1890, "Apparatus for Facilitating Walking, Running, and Jumping," U.S. Patent Nos. 420179, 438830, and 440684.
- [15] Grabowski, A. M., and Herr, H. M., 2009, "Leg Exoskeleton Reduces the Metabolic Cost of Human Hopping," *J. Appl. Physiol.*, **107**(Sept.), pp. 670–678.
- [16] Ferris, D. P., Bohra, Z. A., Lukos, J. R., and Kinnaird, C. R., 2006, "Neuromechanical Adaptation to Hopping With an Elastic Ankle-Foot Orthosis," *J. Appl. Physiol.*, **100**(Jan.), pp. 163–170.
- [17] Farris, D. J., and Sawicki, G. S., 2011, "The Mechanics and Energetics of Human Walking and Running: A Joint Level Perspective," *J. R. Soc. Interface*, **9**(66), pp. 110–118.
- [18] Browning, R. C., Modica, J. R., Kram, R., and Goswami, A., 2007, "The Effects of Adding Mass to the Legs on the Energetics and Biomechanics of Walking," *Med. Sci. Sports Exercise*, **39**(3), pp. 515–525.
- [19] Elliott, G., Sawicki, G., Marecki, A., and Herr, H., 2013, "The Biomechanics and Energetics of Human Running Using an Elastic Knee Exoskeleton," IEEE 13th International Conference on Rehabilitation Robotics (ICORR), Seattle, WA, June 24–26.